molecular pharmaceutics

articles

A Systemic Route for Drug Loading to Lymphatic Phagocytes

**M. I. Papisov,*,[†] A. Yurkovetskiy,[†] S. Syed,[†] N. Koshkina,[‡] M. Yin,[§]
A. Hiller,[†] and A. J. Fischman[†]**

Massachusetts General Hospital, Boston, Massachusetts 02114-2696, Harvard Medical School, Boston, Massachusetts 02115, M. D. Anderson Cancer Center, University of Texas, Houston, Texas 77030, and Nanopharma Corp., Boston, Massachusetts 02116

Received August 28, 2004

Abstract: Lymph nodes are primary germination and proliferation sites for many types of pathogens. Maintaining therapeutic levels of appropriate chemotherapeutic agents in the lymph node tissue is critical for the treatment of both infection and cancer. This study was intended to develop a systemic route for loading lymph node phagocytes with drugs, using a lymph node specific nanocarrier. The latter is assembled as a 10−15 nm particle with a drug-carrying core and a phagocyte-homing poly(1→6)-α-D-glucose based interface. Biokinetics and microdistribution of the model carrier were investigated in vivo. Nanocarrier accumulation in lymph nodes reached 30−35% dose/g in central lymph nodes, with deposition in various phagocytic cell populations. The latter included cells harboring inhaled microparticles translocated to lymph nodes from the lungs. In view of the nanocarrier ability to transport and release significant amounts of various drug substances, the data suggests feasibility of systemic drug loading to lymphatic phagocytes and, through drug release, to the neighboring cells.

Keywords: Lymph node; phagocyte; drug delivery; biodefense; anthrax; cancer

---

Introduction

Lymph nodes are frequently involved in disease, either directly or due to their sentinel role. In particular, lymph nodes can be infected by pathogens translocated to nodes by residential phagocytes. For example, spores of *Bacillus anthracis*, being inhaled and deposited in the lower respiratory tract, are phagocytosed by alveolar macrophages, transported to hilar and mediastinal lymph nodes, and there germinate into vegetative bacilli, producing necrotizing hemorrhagic mediastinitis.[1−3] *Yersinia pestis*, *Francisella tularensis*, and other agents, including HIV, variola, brucella, and others, either are known to have or may have lymph nodes as one of the primary initial development sites.[2] The lymphatic tissues also frequently harbor metastases of several types of cancer.

Since several life-threatening pathologies develop in lymphatic phagocytes or in their near vicinity, the availability of a means for early prophylactic or therapeutic treatment of these cells with appropriate drugs would be of great benefit. Although macromolecules and fine particles are effectively transferred to sentinel nodes after intralymphatic or interstitial administration,[4] central and most peripheral nodes are not reliably accessible through local routes because

---

[*] Author to whom correspondence should be addressed: Department of Radiology, Massachusetts General Hospital, Bartlett Hall 500R, Boston, MA 02114-2696. Tel: (617) 724-9655. Fax: (617) 724-8315. E-mail: papisov@helix.mgh.harvard.edu.

[†] Massachusetts General Hospital and Harvard Medical School.

[‡] M. D. Anderson Medical Center.

[§] Nanopharma Corp.

(1) Inglesby, T. V.; Henderson, D. A.; Bartlett, J. G.; Ascher, M. S.; Eitzen, E.; Friedlander, A. M.; Hauer, J.; McDade, J.; Osterholm, M. T.; O'Toole, T.; Parker, G.; Perl, T. M.; Russell, P. K.; Tonat, K. Anthrax as a Biological Weapon: Medical and Public Health Management (Consensus Statement). *JAMA, J. Am. Med. Assoc.* **1999**, *281*, 1735−1745.

(2) Pile, J. C.; Malone, J.; Eitzen, E. M.; Friedlander, A. M. Anthrax as a Potential Biological Warfare Agent. *Arch. Intern. Med.* **1998**, *158*, 429−434.

(3) Dixon, T. C.; Meselson, M.; Guillemin, J.; Hanna, P. C. Anthrax. *New Engl. J. Med.* **1999**, *341*, 815−826.

10.1021/mp0499149 CCC: $30.25

of the high variability of lymphatic networks. Systemic lymph node loading with drugs, if efficient, would provide a far more reliable therapeutic tool. Another advantage of systemic delivery is the possibility to target all lymph nodes simultaneously (>800 in an adult[5]).

We reported that carbohydrate interfaces assembled of multiple poly(1→6)-α-D-glucose chains direct systemically administered macromolecules and nanoparticles to lymph nodes.[6] This lymph node homing effect allowed us to develop lymphotropic polyglucose-associated nanocarriers. In our previous studies, these agents were successfully utilized to deliver paramagnetic and radioactive diagnostic labels to the intranodal compartments.[7−9]

The goal of this study was to prepare systemic lymph node homing nanocarriers suitable for loading infected lymph node phagocytes with therapeutic agents. The model agents of this study were assembled as graft copolymers of dextran B-512 (essentially poly(1→6)-α-D-glucose,[10] side chains) and polylysine (drug carrying "backbone"). Fluorescent and radioactive labels were linked to the backbone to investigate the in vivo kinetics.

The in vivo transfer of multilabeled preparations were studied by photo- and radionuclide imaging, along with investigation of tissue samples of normal animals and in tumor and focal bacterial inflammation models. Intranodal deposition of the carrier was compared to that of inhaled microparticles translocated to mediastinal nodes from the lungs.

Materials and Methods

Materials. Rhodamine X isothiocyanate (XRITC) and fluorescein isothiocyanate (FITC) were from Molecular Probes Co. (Eugene, OR). Dextran B-512 F (10 kDa), poly-L-lysine hydrobromide, diethylenetriaminepentaacetic acid (DTPA), 1-(3-dimethylaminopropyl)-3-ethylcarbodiimide (EDC), sodium *m*-periodate, sodium 2,4,6-trinitrobenzenesulfonate (TNBS), Sepharose, Sephacryl, and Sephadex gels, and other reagents and solvents, all of at least analytical grade, were from Sigma Chemicals (St. Louis, MO). Carrier-free [^{111}In]InCl$_3$ was from NEN Dupont and Perkin-Elmer (MA).

Male Sprague Dawley CD rats and female Fisher 344 rats were from Charles River Laboratories (Wilmington, MA); male New Zealand White rabbits were from Millbrook Farms (Amherst, MA).

Equipment. Preparative isolation and purification of polymers and polymer conjugates was carried on a G-25 gel SpectraChrom (60 cm × ID 10 cm) column equipped with a Milton Roy (Rochester, NY) liquid delivery system, MasterFlex CL peristaltic pump, Knauer-2401 RI detector, Foxy JR fraction collector, and Varian-Prostar data acquisition system. A QuixStend flow dialysis system (A/G Technology, Needham, MA) was used in high-volume procedures. Diafiltration (ultrafiltration) cells and membranes used in low-volume separations were from Amicon (Bedford, MA). Particle size analysis was carried out using Coulter N4 MD and Brookhaven ZetaPlus analyzers (Coulter, Fullerton, CA; Brookhaven Instruments, Holtsville, NY). The 1282 Compugamma CS counter was from LKB (Bromma, Sweden). Spectral equipment was from Varian, Inc. (Palo Alto, CA) (300Bio UV−visible spectrophotometer equipped with thermostated multicell Peltier block) and Photon Technologies International (Lawrenceville, NJ) (modular TimeMaster/Quantamaster fluorescence spectrometer with thermostated sample holder). Size exclusion chromatography (SEC) in aqueous media was carried out using a Varian-Prostar HPLC system equipped with a BIO-RAD model 1755 refractive index detector and LDC/Milton Roy SpectoMonitor 3000 UV detector. In separations involving radiolabeled preparations, an additional high-sensitivity custom γ detector was used. HPSEC Biosil SEC-125 and Biosil SEC-400 (BIO-RAD) and low-pressure Superose-6 (Pharmacia) columns were used for size exclusion chromatography at 1 mL/min. SEC column calibration was performed based on broad molecular weight dextran and protein standards.

A Sigma 410 γ camera (Ohio Nuclear, Solon, OH) equipped with a medium-energy parallel hole or 3 mm pinhole collimator was used for radionuclide imaging. Photoimaging was carried out using a Nikon TE300 Quantum microscope equipped with Plan Fluor ELWD objectives and Diagnostic Instruments Spot RT Slider CCD camera (Nikon Instruments Inc., Melville, NY; Diagnostic Instruments, Sterling Heights, MI).

Synthesis of Lymphotropic Nanocarriers. The synthetic procedure used in this study was developed to assemble carrier particles that are (i) smaller than 20 nm in total (hydrodynamic) diameter, (ii) surrounded by a brush of polyglucose (dextran B-512) chains, and (iii) contain a drug loadable core/backbone. In this study, the poly-L-lysine backbone was labeled with a fluorescent dye and a radionuclide. Poly-L-lysine was selected as a backbone material due to the multiple amino groups that are suitable for linking

---

(4) Charman, W. N., Stella, V. I., Eds. *Lymphatic transport of drugs*; CRC Press: Boca Raton, 1999.

(5) Som, P. Lymph nodes of the neck. *Radiology* **1987**, *165*, 593−607.

(6) Papisov, M. I.; Bogdanov, A. A., Jr.; Schaffer, B. K.; Nossiff, N.; Shen, T.; Weissleder, R.; Brady, T. J. Colloidal magnetic resonance contrast agents: effect of particle surface on biodistribution. *J. Magn. Magn. Mater.* **1993**, *122*, 383−386.

(7) Papisov, M. I.; Weissleder, R.; Brady, T. J. Systemic lymph node targeting with macromolecular imaging agents. In *Handbook of Targeted Delivery of Imaging Agents*; Torchilin, V. P., Ed.; CRC Press: Boca Raton, 1995.

(8) Harika, L.; Weissleder, R.; Zimmer, C.; Poss, K.; Papisov, M.; Brady, T. J. MR lymphography with a lymphotropic T1-type MR contrast agent: Gd-DTPA-carrier. *Magn. Res. Med.* **1995**, *33*, 88−92.

(9) Harika, L.; Weissleder, R.; Poss, K.; Papisov, M. A macromolecular intravenous agent for MR lymphography: characterization and efficacy studies. *Radiology* **1996**, *198*, 365−370.

(10) Jeanes, A. Immunochemical and related interactions with dextrans reviewed in terms of improved structural information. *Mol. Immunol.* **1986**, *23*, 999−1028.

the backbone with other components (carbohydrate chains, labels, and drug molecules).

The synthetic scheme included two stages: backbone formation (partial modification of polylysine with fluorescent labels and DTPA) and subsequent backbone association with multiple dextran molecules. Each stage was optimized in our previous studies to obtain a minimally cross-linked soluble graft copolymer containing sufficient amounts of dextran B-512, labels, and/or model drugs.

Poly-L-lysine hydrobromide (MW 50 kDa, average polymerization degree 191) was dissolved in a minimal amount of 0.1 M sodium borate (pH = 9.3). Then, 5% XRITC solution in DMSO was added in the amount necessary to modify 0.5% (in one experiment, 10%) of the polylysine amino groups. After a 60 min incubation at 25 °C, labeling efficacy, as determined by size exclusion chromatography (SEC), was near 100%.

To conjugate the XRITC-labeled polylysine with DTPA, the polymer was dissolved in a 20-fold molar excess of 1 M $Na_{2.7}$DTPA, pH = 7.6. Then, EDC, 0.95:1 mol/mol to lysine monomer, was added at 5 °C. The temperature was allowed to rise to ambient with stirring, and after a 10 h incubation the resultant poly-L-lysine(XRITC)(DTPA) was desalted on Sephadex G-25 and lyophilized. The effective extinction coefficients of the polymer at the absorbance peaks of the fluorescent dyes used in the syntheses were determined.

Dextran B-512 was oxidized by $NaIO_4$ (0.2 mol/mol by monomer) and desalted by flow dialysis. The resultant aldehyde-dextran was conjugated with the backbone polymer, poly-L-lysine(XRITC)(DTPA), at a dextran concentration of 50 g/L and a dextran:polylysine molar ratio of 400:1, in the presence of a 2-fold excess of potassium cyanoborohydride. After a 24 h incubation, the resultant graft copolymer was isolated by flow dialysis (300 kDa cutoff), additionally desalted by gel chromatography (Sephadex G-25/water), and lyophilized. The effective extinction coefficients were determined as described above.

Self-quenched carriers overloaded with FITC and XRITC, in which fluorescence was 95−99% suppressed by FRET, were prepared analogously using polylysine backbones with high (20%) fluorophore content.

Nanocarrier Characterization. Carrier size, composition, and structure were investigated as follows.

Carrier size was determined by size exclusion HPLC and photon correlation laser light scattering (PCLS) in water, at 2 mg/mL. All samples were filtered through a 0.1 μm nylon membrane.

PCLS was carried out at a 90° beam angle, 3 μs sampling time, and 5−10 min acquisition time. The "size distribution processor" (SDP) analysis (Coulter N4 MD workstation) was performed in the 1−100 nm range. The hydrodynamic size of the carrier was 10−12 nm. Carrier saturation with gadolinium (to increase nanoparticle core refraction) resulted in the prevalence of a 6.3 ± 1 nm population, which is most likely the size of the gadolinium-saturated core compartment. PCLS with a 1 μs sampling time showed independent motions of a small (1 nm) component. This "small component" could not be separated from the carrier by HPLC or continuous dialysis; therefore, the "small component" motions were interpreted as independent conformational changes of dextran chains attached to the backbone.

HPLC elution was performed isocratically with 50 mM phosphate buffered 0.9% NaCl, pH = 7.0. Sample volume: 10−100 μL depending on polymer concentration (loop volume 1 mL). The elution time by size exclusion chromatography corresponded to a carrier diameter close to a 750 ± 350 kDa spherical protein (i.e., about 12 ± 3 nm), regardless of gadolinium content.

DTPA content (chelating capacity) was measured by relaxometric titration. The method is based on the higher gadolinium relaxivity in a polymer-bound form than in low molecular weight complexes, due to the restrictions in the gadolinium ion reorientation rate. Accuracy of the method was validated by gadolinium analysis (performed by Galbraith Laboratories, Knoxville, TN). Standard 0.25 mM gadolinium solution in 0.01 M citrate buffer (pH = 6) was placed into 1 mL test tubes. Relaxation times (T1 and T2) of the standard solution were measured at 37 °C. Then, a solution containing a known amount of the carrier was gradually added to the standard solution in 2 or 5 μL aliquots. Relaxation times were determined 1 min after each addition. Results were plotted as relaxation time (T) and inverse relaxation time against the added amount of the carrier. Polymer capacity was determined by identifying an equivalency point.

Amino group, DTPA, and fluorescent dye content in the backbone polymer and in the final product were monitored during the syntheses. The TNBS reaction with the residual amino groups of the DTPA-modified polylysine showed 83 ± 3% substitution, i.e., 158 ± 3 DTPA molecules per average polylysine chain. The extinction coefficients of polylysine-XRITC, polylysine-XRITC-DTPA and the final carrier were 2.74 ± 2, 0.76 ± 0.08, and 0.19 ± 0.09 (cm mg/mL)$^{-1}$ respectively. Assuming that DTPA was present in the polymers in the form of its disodium salt, these numbers corresponded to 154 ± 15 DTPA moieties and 28 ± 3 average dextran molecules (MW = 10 kDa) per polylysine chain. Dextran content as measured using the phenol/sulfuric acid reaction[11] was 22 ± 4 average dextran molecules per average polylysine backbone. Since oxidized hexose units do not form colored products with phenol (as determined in a separate experiment), the latter value should be corrected to 24 ± 4 dextran chains per backbone. This value may be an underestimate because steric hindrance of the backbone by dextran chains at the final stage of grafting could result in the selection of smaller dextran molecules (as a result, the same polysaccharide content may correspond to a larger number of smaller dextran chains per backbone).

The chelating capacity of DTPA-polylysine (1.63 ± 0.08 μmol/mg) and the final carrier (0.24 ± 0.1 μmol/mg), as

---

(11) Dubois, M.; Gilles, K. A.; Hamilton, J. K.; Rebers, P. A.; Smith, F. Colorimetric method for determination of sugars and related substances. *Anal. Chem.* **1956**, *28*, 350−356.

estimated by relaxometric titration, was in agreement with the substitution degree determined by other methods (152 ± 8 DTPA moieties per average molecule). The chelating capacity of the final product appeared lower (82 ± 1 DTPA groups per molecule), which may be a result of partial DTPA blockage by metal ions (impurities present in the large volume of chelator-free buffer solutions used at the last stage of carrier isolation).

Total carrier yield at the last stage, as measured by the optical density at the XRITC absorbance peak, was 80%. Losses were attributed mainly to the flow dialysis process, where the low molecular weight subfraction partially escaped through the filter pores (considering the 10−11 nm pore diameter).

Interface Permeability (via Relaxivity of Carrier-Bound Gadolinium). Relaxivity was determined from the regression of inverse relaxation time vs gadolinium concentration, using serial dilutions of Gd−carrier complex obtained as described above (DTPA content investigation).

Gadolinium chelated by the DTPA groups of the carrier demonstrated high relaxivity in water, $R1 = 17.3 \pm 0.3$ mM^{-1} s^{-1} and $R2 = 19.7 \pm 0.3$ mM^{-1} s^{-1} at 0.47 T and 37 °C. High relaxivity evidenced, on one hand, that the rotational diffusion (reorientation) of gadolinium ion was restricted due to its attachment to the relatively rigid carrier backbone. On the other hand, this effect could not take place if water diffusion to/from the backbone was restricted; therefore, the carbohydrate interface was easily permeable for small molecules (being, physically, a "brush").

Radionuclide Labeling. Model preparations were labeled with ^{111}In (0.1−10 mCi/mg) by transchelation from indium citrate at pH = 5.6. The remaining DTPA groups were saturated with calcium to avoid hypometalemia in the experimental animals. Labeled carriers were purified by size exclusion chromatography (radiochemical purity >98%).

Animal studies were performed in accordance with the institutional guidelines. Animals were anesthetized with pentobarbital (35 mg/kg intravenously) and given supporting doses (10 mg/kg) when necessary.

The radiolabeled preparations were injected into the tail vein (rats) or marginal ear vein (rabbits). Planar scintigraphic images were acquired immediately after carrier administration to monitor possible extravasation via vascular perforation at the injection site. Animals with more than 1% extravasation were excluded from the study to avoid data distortion caused by local lymphatic drainage.

Biokinetics was studied in 33 normal 240 ± 15 g CD rats, at a carrier dose of 1.2 mg/kg. Animals, $n = 3$ per group, were euthanized at 1, 2, 3, 4, 5, 6, 7, 8, 10, 11, and 21 h after administration. Injection quality was monitored by γ-scintigraphy. Popliteal and paraaortic nodes of animals with minor PGM extravasations at the injection site were excluded from the experiment to avoid data distortion due to local lymphatic drainage (2, 4, 10, 11 and 21 h groups; one animal from each). Tissue samples (lymph nodes, liver, spleen, muscle, kidney, heart, thyroid, bone, blood, lung, testes, tail) were collected and counted. Data was corrected for radonuclide decay.

Since biological activity of a drug in a certain tissue depends on the drug concentration in that tissue, results were presented as specific accumulation (percent of injected dose per gram of tissue).

Dose dependence of the biokinetics was studied in 24 normal 390 ± 20 g CD rats. Radiolabeled preparations were administered at 1.8 μg/kg, 14 μg/kg, 0.12 mg/kg, 2.6 mg/kg, 12.7 mg/kg, and 63.3 mg/kg into the tail vein; $n = 4$ per dose. Blood samples were acquired through tail veins opposite to the veins used for injection. Animals were euthanized 24 h after administration, and tissue samples were collected and studied as described above.

Carrier microdistribution in lymph node (and other) tissues was studied by photoimaging. Fluorescent preparations (1−20 mg/kg) were injected into the tail vein of eight 200 ± 10 g CD rats and 10 400 ± 20 g CD rats. Tissues were collected 24 h after the administration and cryotomized. Tissue slices (15 μm) were studied immediately, without fixation and staining.

In Vivo Transfer Routes. To discriminate between the two possible mechanisms of deposition in lymph nodes (intranodal phagocytosis and extranodal phagocytosis with subsequent phagocyte translocation to lymph node), two carrier preparations, one labeled with FITC and the other with XRITC, were administered with a 48 h interval. The intranodal phagocytosis was expected to result in a mixed accumulation of both labels in the same phagocytes. An abundance of cells containing only one label would suggest that these cells had contacted only one of the preparations and, therefore, were transferred to lymph nodes from the outside after carrier uptake.

Biokinetics in Inflammation and Tumor Models. To evaluate the potential biodistribution sensitivity to local pathologies, carrier was administered to animals with model inflammation (rabbit) and tumor (rat). Two normal rabbits and four rabbits with focal inflammation were used in the scintigraphic studies. Focal bacterial inflammation was induced in four rabbits by intramuscular inoculation of a single clinical isolate of *Staphylococcus aureus* as previously described.[12] Bacterial suspension, 10^9 cells/ml, 1 mL, was injected into one hind leg. Carrier preparation (19 mg/kg) was injected 24 h after inoculation through the marginal ear vein. Scintigrams were acquired 24, 48, and 96 h after the carrier injection. Mammary adenocarcinoma (MAC) was implanted in the front and rear extremities (unilaterally) of 8 Fisher rats (300 ± 30 g), 2 mm^3 of R3230 MAC tissue per animal. The carrier was administered intravenously 10 days after cancer induction, when tumor size reached ca. 1 cm.[3] Scintigraphy and biodistribution studies were performed as described above.

---

(12) Fishman, A. J.; Pike, M. C.; Kroon, D.; Fucello, A. J.; Rexinger, D.; tenKate, C.; Wilkinson, R.; Rubin, R. H.; Strauss, H. W. Imaging focal sites of bacterial infection in rats with 111-In-labeled chemotactic peptide analogs. *J. Nucl. Med.* **1991**, *32*, 483−491.

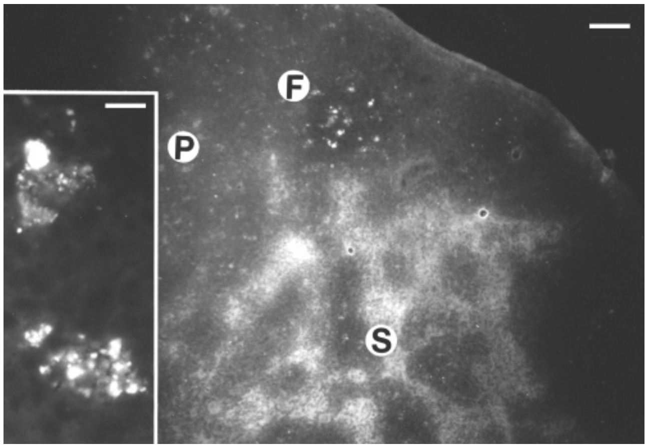

Figure 1. Microdistribution of a fluorescent lymphotropic nanocarrier S-03 in rat lymph node 24 h after intravenous administration. F: follicle. P: paracortex. S: sinus. Bar: 100 μm. Inset: Intracellular distribution in paracortical phagocytes (bar: 15 μm). Fluorescence photoimaging, unstained, unfixed 20 μm cryosection, ×10 air and ×100 oil objectives.

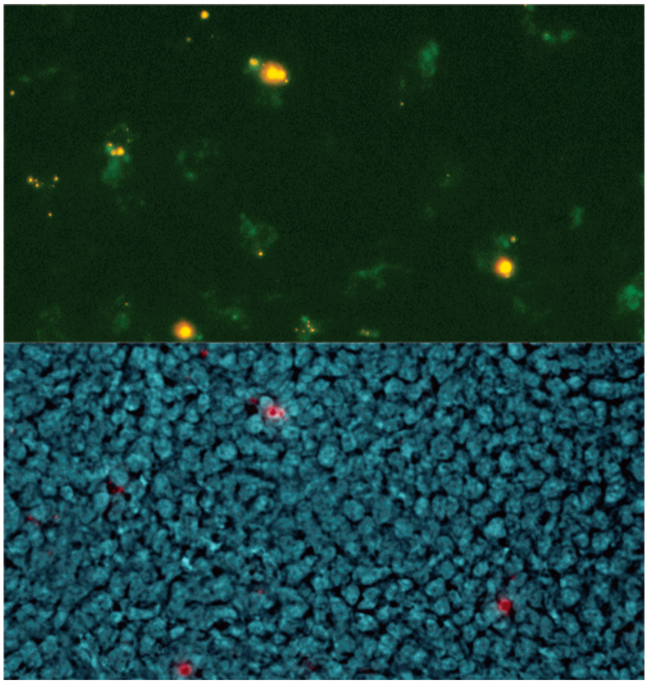

Figure 2. (A) (top) Coaccumulation of inhaled aerosolized microparticles (red) and intravenously injected nanocarrier (green) in mediastinal lymph node of a normal rat. Field: 193 × 145 μm. (B) (bottom) Same region, overlay of red channel fluorescence and phase contrast image.

Carrier Colocalization with Inhaled Particles. To label lung phagocytes that would ingest and translocate airborne spores or bacteria to lymph nodes, fluorescent microparticles were used as a proxy for the bacterial spores. Nonbiodegradable polystyrene microparticles stained with Nile Red (0.07 μm, Interfacial Dynamics Inc.) were administered as an aerosol in 0.9% saline to normal rats. Particle suspension (2 mg/mL) was aerosolized using an Aerotech-II nebulizer (CIS-USA) at 50 psi without flow control (intrinsic air flow ca. 10 L/min, suspension flow 1 mL/min). Aerosol was delivered directly to a custom 2-gal acrylic chamber. In this chamber, rats ($n = 3$ per group) were exposed for 10 min to the flow of aerosol.

Three days after the exposure to microparticles, the model FITC-labeled nanocarrier was injected intravenously (tail vein) at 0.3 mg/kg. Animals were euthanized 48 h postinjection. Mediastinal lymph nodes and other tissues were harvested and cryotomized (slice thickness 14 μm). Control samples of thoracic lymph node tissue were taken from (a) untreated rats and (b) rats treated only with particle aerosol.

Unstained, unfixed tissue slices were studied by photoimaging. Images were registered in red and green channels (HQ FITC and HQ TRITC filters, CCD: grayscale unfiltered), at a preset exposure time (equal for either channel). Phase contrast images were acquired with automatic exposure.

Fluorescence images were processed using NIH Image software to obtain fluorescence intensity maps. The image shown in Figure 2A was composed by combining unedited red and green grayscale bitmaps in the red and green channels of an RGB image, respectively.

Results

Carrier Microdistribution in Lymph Node Tissues. Photoimaging demonstrated label deposition in cells morphologically identical to essentially all previously described[13] phagocytic populations of rat lymph node, which can be distinguished from surrounding lymphocytes by characteristic morphologies and positioning.[14] Major carrier accumulating cell groups included cells lining marginal and medullar lymphatic sinuses, medullar and large intrafollicular macrophages, and paracortical phagocytes (Figure 1). The label was predominantly concentrated in vesicular compartments (Figure 1, inser). No vesicular label accumulation was found in lymphocytes. Control node tissue samples (carrier not injected) had no detectable fluorescence.

Injection of a nonfluorescent self-quenched carrier overloaded with XRITC resulted in the development of a similar fluorescence pattern within 48 h. This can be attributed to label release from the macromolecule followed by diffusion in tissues, which prevented the quenching energy transfer. Therefore, the carrier was, most likely, accumulated and degraded in the lysosomal compartment.

In the marginal lymphatic sinuses, fluorescence was increased at areas adjacent to the openings of afferent lymphatics, indicating that at least a fraction of the carrier arrived with lymph. Diffuse fluorescence was also observed in the walls of some of the high endothelial venules (HEV), which, in light of the known HEV permeability,[15] may indicate direct passage from blood.

---

(13) Fossum, S. The architecture of rat lymph nodes. II. Lymph node Compartments. *Scand. J. Immunol.* **1980**, *12*, 411−420.

(14) Fossum, S.; Ford, W. L. The organization of cell populations within lymph nodes: their origin, life history and functional relationships. *Histopathology* **1985**, *9*, 469−499.

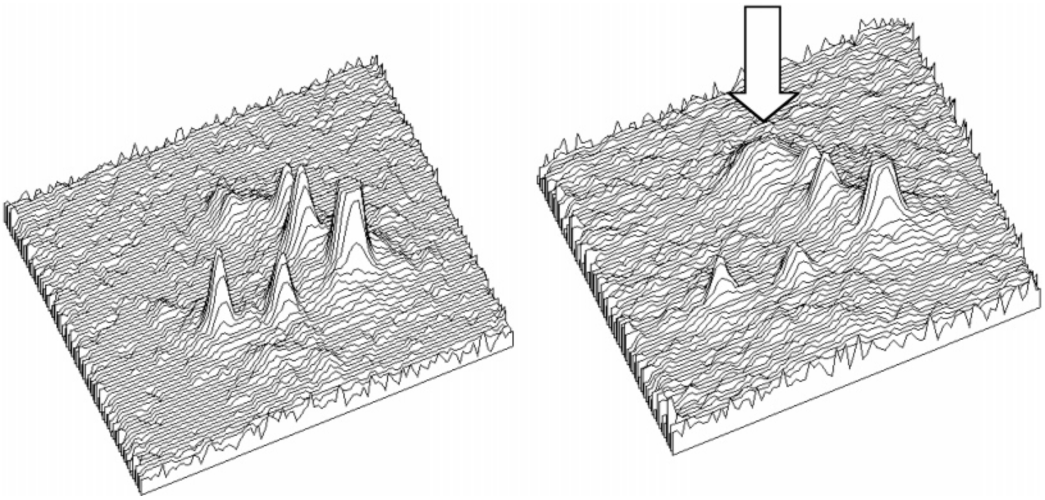

Figure 3. Fluorescence intensity profiles for a single cell: red (left) and green (right) channels. The difference in fluorescence intensity distribution is clearly seen (arrow), suggesting the presence of both the inhaled microparticles and the intravenously administered nanocarrier in different compartments of the same cell.

The pattern of carrier accumulation in spleen was similar to that of lymph nodes, with significant label deposition in phagocytes. In liver tissue, label accumulated in Kupfer cells as well as in hepatic endothelium.

Administration of FITC-labeled carrier followed (48 h later) by XRITC-labeled carrier showed mixed label accumulation in the same cells. Cells containing only fluorescein or only rhodamine X were not found, which was consistent with carrier uptake within lymph node tissues, rather than with extranodal uptake and subsequent translocation to lymph nodes.

Coaccumulation of Inhaled Microparticles and Intravenously Administered Carrier. Photoimaging of mediastinal (parabronchial) lymph nodes after the iv administration of fluorescein-labeled carrier and inhalation of Nile Red labeled microparticles showed that the particles and the carrier accumulated not only in close proximity to each other but actually in the same cells (Figure 2). Although Nile Red has a broad emission spectrum that significantly "leaks" into the fluorescein channel, image analysis with NIH Image software clearly showed that green and red emission profiles from individual cells are significantly different (Figure 3), which suggests different label compartmentalization within the cell. Most likely, the nonbiodegradable Nile Red latex particles are concentrated in lysosomes and small vacuoles, while fluorescein is at least partially cleaved from the biodegradable carrier and thus present in other intracellular compartments.

Control studies demonstrated absence of lymph node fluorescence in animals that received no aerosol and no nanocarrier, and only red fluorescence in animals that were exposed only to particle aerosol (not shown). Interestingly, isolated phagocytes containing Nile Red stained particles were found not only in mediastinal lymph node groups but, although in much smaller numbers, in other central and peripheral lymph nodes. These cells were also loaded with the carrier.

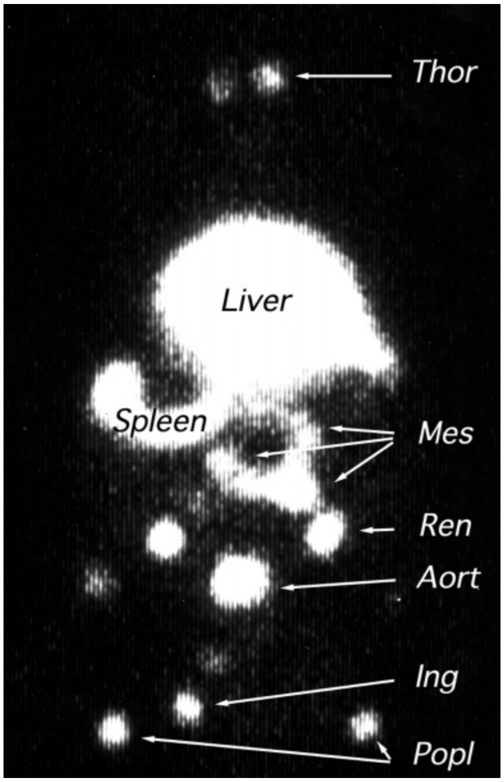

Figure 4. Whole-body scintigram of a rat 24 h after iv administration of ^{111}In labeled nanocarrier, 100 μCi/kg. Anterior view (acquired using a pinhole collimator and thus inverted). Lymph nodes: mediastinal (Thor), mesenteric (Mes), paraaortic (Aort), pararenal (Ren), inguinal (Ing), popliteal (Popl).

Radionuclide Imaging and Biokinetics in Normal Animals. Carrier transfer in normal animals after intravenous administration was studied by dynamic scintigraphy and

---

(15) Anderson, A. O.; Anderson, N. D. Studies on the structure and permeability of the microvasculature in normal rat lymph nodes. *Am. J. Pathol.* **1975**, *80*, 387−418.

Table 1. Carrier Biodistribution in Rats after Intravenous Administration of 1.2 mg/kg ^{111}In-Labeled Preparation (% of Injected Dose/g of Tissue)[a]

time, h:	1	2	3	4	5	6	7	8	10	11	21
blood	3.71	2.77	2.16	1.65	1.34	1.32	1.57	0.93	0.68	0.41	0.06
liver	1.79	2.32	2.42	3.14	3.34	3.33	3.34	2.74	3.49	3.98	3.52
spleen	1.43	2.43	5.31	5.49	6.66	3.53	7.21	4.77	6.91	7.69	11.64
muscle	0.05	0.04	0.09	0.05	0.06	0.04	0.04	0.04	0.05	0.03	0.04
heart	0.37	0.31	0.38	0.29	0.27	0.28	0.26	0.26	0.23	0.16	0.15
kidney	0.76	0.71	0.7	0.66	0.66	0.7	0.7	0.65	0.84	0.87	1.13
thyroid	0.16	0.16	0.08	0.12	0.07	0.09	0.08	0.07	0.08	0.06	0.05
bone	0.37	0.42	0.4	0.42	0.27	0.44	0.34	0.37	0.32	0.32	0.4
lung	0.76	0.67	0.55	0.39	0.36	0.32	0.36	0.32	0.25	0.15	0.09
testes	0.13	0.19	0.19	0.2	0.2	0.53	0.18	0.18	0.24	0.23	0.26
LN popliteal	0.61	1.34	3.29	3.2	2.42	5.96	1.92	2.86	10.82	37.64	18.62
LN paraaortic	0.74	3.78	2.31	5.45	4.88	15.8	8.35	13.44	50.96	39.04	26.75
LN mesenteric	3.81	6.64	9.11	13.02	20.99	19.88	24.95	15.96	22.48	23.3	18.59
LN axillary	0.33	0.33	0.43	0.59	0.99	1.56	2.24	0.84	1.77	5.09	0.58
LN cervical	0.32	0.58	1.32	1.74	2.38	1.23	1	3.87	3.82	0.62	0.9

[a] Tissue samples were counted at 1−21 h after the injection, 3 animals per point. Average standard deviations: peripheral lymph nodes, 60 ± 7%; mesenteric lymph nodes, 28%; other tissues, 22 ± 7%.

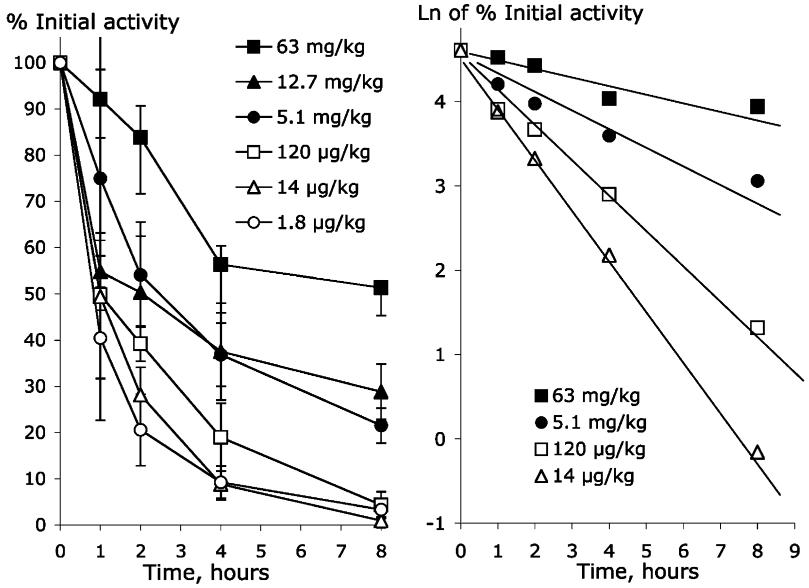

Figure 5. Nanocarrier blood clearance in rats as a function of injected dose. Left: average values (bars: standard deviations). Right: data linearization in semilogarithmic coordinates, individual animals.

tissue sampling. The images showed continuous carrier presence in blood and slow accumulation in liver, spleen, and lymph nodes. Label transfer to the bladder was negligible. Label accumulation in lymph nodes of the mesenteric group was evident in high-resolution images (pinhole collimator) as early as at the fourth hour after carrier administration in rats, and at about 24 h in rabbits. Peripheral lymph nodes became visible at 6−12 h after carrier injection in rats and at 12−24 h in rabbits. By 24 and 48 h in rats and rabbits, respectively, scintigrams clearly demonstrated significant label accumulation in both central and peripheral lymph node groups (Figure 4). The label distribution pattern did not change over the next 2−4 days. Label accumulation highly varied from node to node. Contralateral lymph nodes of the same animal often demonstrated significantly (1.5−3 times) different label accumulation; for example, note the difference between contralateral lymph nodes in Figure 4. Also note that a major fraction of the injected dose accumulated in the liver. However, due to the large mass of the liver tissue in which the carrier is distributed, compared to the mass of a node (typically, 11 ± 1 g vs 5−50 mg in a 240 g rat), concentration of the carrier in the node tissue is by 1−2 orders of magnitude higher than in the liver (see below).

Carrier biokinetics after intravenous administration was studied at 1.2 mg/kg by blood and tissue sampling and radioactivity registration on a γ counter.

As expected, renal filtration was negligible. Blood clearance and accumulation in liver and spleen were slow and essentially monoexponential (Table 1). However, the half-

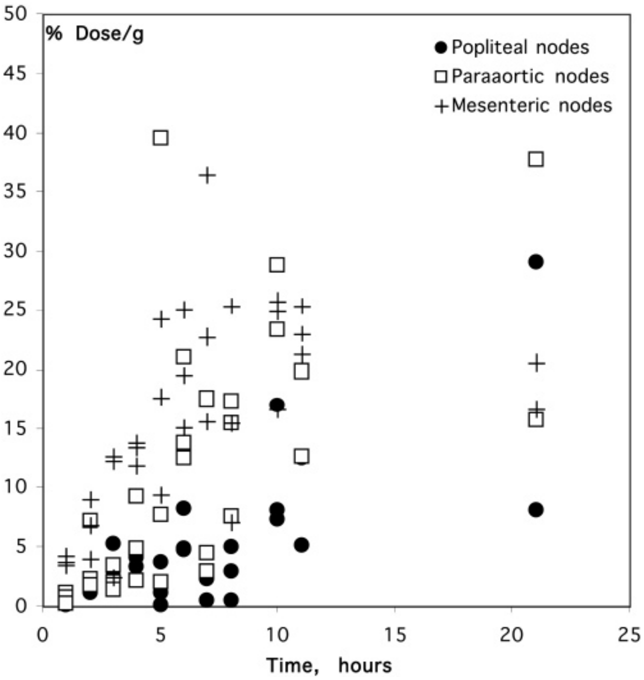

Figure 6. Carrier accumulation in lymph nodes at 1.2 mg/kg (individual nodes).

life consistently increased with the injected dose (Figure 5), which suggests a more complex nanoparticle clearance mechanism than the previously described true first-order process.[16]

Due to the high individual variations in carrier uptake among lymph nodes (SD > 50% of the mean value), it was impossible to determine from the kinetics of carrier uptake in lymph nodes whether the lymphatic uptake was monoexponential (Figure 6), which would correspond to direct carrier transfer from blood. Accumulation in peripheral nodes apparently had a lag period, which could be indicative of an intermediate transfer process (most likely interstitial transfer and lymphatic transport[17]). The latter would be in agreement with increased carrier accumulation in lymph nodes near the efferent lymphatics. Possibly, both transfer mechanisms are present, which is to be determined in our future studies.

Biodistribution was found to be dose-dependent (Figure 7). At all but the lowest dose (1.8 μg/kg) the lymphatic accumulation was significant. Other tissues accumulated considerably lower amounts of the carrier (Table 1). Splenic and nodal accumulation were maximal between 0.1 and 10 mg/kg. In contrast, hepatic specific accumulation was independent of dose within the entire dose range (5 orders of magnitude), which shows significant differences in cell interactions with the carrier in liver vs lymph nodes and spleen.

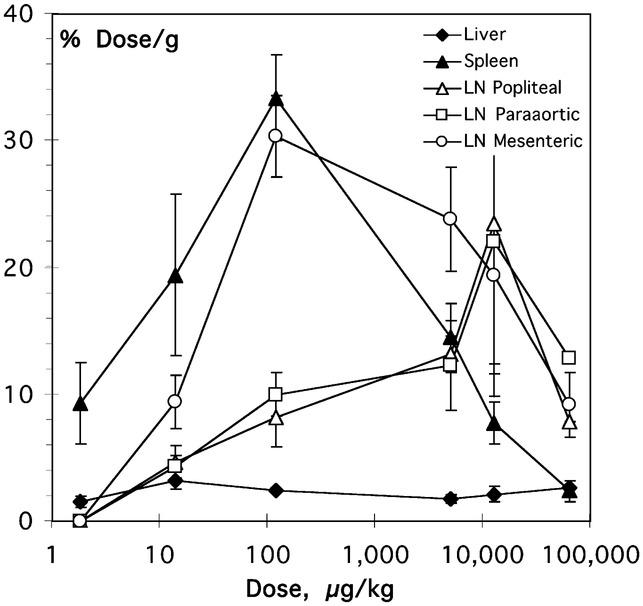

Figure 7. Dose dependence of the nanocarrier biodistribution in rats (see text).

At all doses, central lymph nodes accumulated higher label amounts than peripheral lymph nodes. However, at the highest injected doses, an increased accumulation was observed in some rats in lymph nodes draining extremities (see Figure 7). This is most likely due to the paw edema which occurs in some rats after injection of large amounts of dextran-based preparations.[18] Dextran sensitivity, however, is not the underlying mechanism of the lymphatic uptake of polyglucose-modified nanoparticles, since the uptake of dextran B-512 preparations in lymph nodes was also observed in rats that are not dextran-sensitive, as well as in mice, rabbits, and other animals and humans.

Carrier Biodistribution in Inflammation and Tumor Models. In all animals, hyperplastic sentinel nodes draining either focal bacterial inflammation (rabbit) or growing nonmetastatic mammary adenocarcinoma R3230 (rat) demonstrated higher carrier accumulation than analogous contralateral lymph nodes.

Rabbit lymph nodes have been semiquantitatively assessed by static scintigraphy via radiation counting over regions of interest. Scintigraphy (Figure 8 A) showed a 4−7-fold increase in the inflammation-draining nodes.

Rat lymph nodes draining adenocarcinoma (Figure 8B) were additionally assessed by tissue counting at 24 h after carrier administration. The sentinel tumor draining nodes showed significantly ($p < 0.025$) higher accumulation than normal contralateral lymph, 148 ± 36 kcpm per node vs 36 ± 24 kcpm, respectively, (average ± standard deviation for 8 animals).

---

(16) Papisov M. I.; Savelyev V. Y.; Sergienko V. B.; Torchilin V. P. Magnetic drug targeting (I) In vivo kinetics of radiolabelled magnetic drug carriers. *Int. J. Pharm.* **1987**, *40*, 201−206.

(17) Papisov, M. I. Modeling in vivo transfer of long-circulating polymers (two classes of long circulating polymers and factors affecting their transfer in vivo). *Adv. Drug Delivery Rev.* **1995**, *16*, 127−139.

(18) West, G. B. Heparin and dextran anaphylactoid reactions in rat. *Int. Arch. Allergy Appl. Immunol.* **1983**, *70*, 373−375.

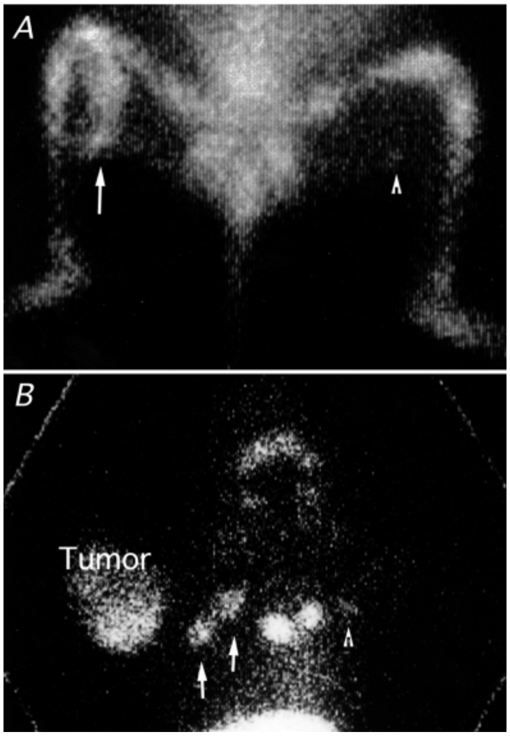

Figure 8. Nanocarrier distribution 24 h after iv administration in animals with model pathologies. γ scintigraphy, pinhole collimator. (A) Rabbit, rear extremities, bacterial inflammation (left leg, outlined by label accumulation). Note significant difference in label accumulation in the sentinel node (arrow) and normal contralateral node (arrowhead). (B) Rat, from head (top) to liver (bottom). Tumor (left extremity, outlined by diffuse label accumulation). Note high carrier accumulation in the axillary sentinel nodes (arrows) compared to the contralateral nodes (arrowhead).

In both models, carrier accumulation in the pathological tissue is most likely related to the enhanced permeability and retention (EPR) effect: accumulation of macromolecules and nanoparticles in tissue zones with high endothelial permeability.[19]

Discussion

The data demonstrated that intravenously administered lymph node specific nanocarrier accumulated in mediastinal lymph nodes inside as well as in the near vicinity (0−50 μm) of phagocytes harboring inhaled microparticles. Significant accumulation was also observed in all other lymph node groups, in all intranodal phagocyte populations.

The carrier structure was developed to transport a variety of drug substances in a sterically protected internal core; our earlier studies showed that high drug loads do not significantly affect biodistribution. The nanocarrier used in this study consisted of particles (formally, individual soluble graft copolymer molecules) containing, on average, one polylysine backbone, 24 dextran B-512 molecules, and 150 DTPA groups per particle. A non-cross-linked graft copolymer of this composition has a molecular mass of ca. 335 kDa.

The "size" of a graft copolymer is, essentially, not a strictly defined parameter due to the absence of a clearly defined physical boundary. The "full" hydrodynamic size, including side chains, as determined by size exclusion chromatography, was 12 ± 3 nm. Size as measured by photon correlation LLS was 6.3 ± 1 nm (metal-saturated) to 12 nm (unsaturated). The former number should be ascribed to the relatively rigid, highly scattering core compartment, excluding the flexible side chains, which can be registered in LLS as independently moving objects. The 12 ± 3 nm hydrodynamic diameter suggests that carbohydrate chains are significantly coiled, otherwise the size would be closer to 20 nm. On the other hand, the interface permeability to small molecules suggests that side chains in the carrier were not completely collapsed. Therefore, the nanocarrier of this study is best described physically as a flexible brush of coiled polyglucose molecules, ca. 10−15 nm in diameter, with a relatively rigid 6−10 nm "core".

We have shown previously that carbohydrate brush permeability for large molecules is limited. For example, dextran chains reduced the rate of immunoglobulin interaction with a backbone-bound antigen by approximately 10-fold.[21] The nonspecific interactions of the polylysine core with the environment have been suppressed even more efficiently, by 3 orders of magnitude.[20] This efficient steric protection enables low dependence of carrier pharmacokinetics on the inner content, and makes the carrier capable of transporting a variety of compounds. For example, our previous studies showed that biodistributions of rhodamine (10% w/w) and doxorubicin (12%) loaded carriers, as well as particles with solid iron oxide cores, did not significantly differ from biodistribution of unloaded carrier.[7,22]

The biokinetics and microdistribution data suggested that the model carriers reached the intranodal compartments via extravasation either in tissues (with subsequent lymphatic drainage) or inside lymph nodes. Most probably, both pathways were present, although their role may vary as a function of changing intra- and extranodal endothelial permeability. At this point, high variations between individual nodes (e.g., average standard deviation in carrier accumulation 59 ± 6% in peripheral nodes in a group of 32 animals) do not allow data correlation with mathematical models.

---

(19) Maeda, H.; Seymur, L. W.; Miyamoto, Y. Conjugates of anticancer agents and polymers: advantages of macromolecular therapeutics in vivo. *Bioconjugate Chem.* **1992**, *3*, 351−362.

(20) Papisov, M. I.; Martin, C.; Poss, K.; Weissleder, R.; Brady, T. J. Amplification of steric effects in cooperative systems. *Proc. Int. Symp. Controlled Release Bioact. Mater., 22nd* **1995**, 442−443.

(21) Papisov, M. I.; Poss, K.; Weissleder, R.; Brady, T. J. Intravenous lymphotropic polymers: the SPAR effect. In *Proceedings of the Society of Magnetic Resonance*; 2-nd meeting, San Francisco, CA; SMR: Berkeley, CA, 1994; p 388.

(22) Poss, K.; Bogdanova, A. V.; Weissleder, R.; Brady, T. J.; Papisov, M. I. Cytotoxicity of doxorubicin covalently linked with the backbone of lymphotropic graft copolymers. In *Seventh international symposium on recent advances in drug delivery systems, Abstracts*; Salt Lake City, UT, 1995; University of Utah: Salt Lake City, 1995; pp 173−174.

Carrier biodistribution demonstrated a potentially useful sensitivity to the lymph node state. Local inflammations and lymph node reaction to antigens can induce dramatic changes in vascular permeability, lymph flow, lymph node size, and intranodal phagocyte activity.[23] All these factors could be expected to affect carrier biodistribution, and result in a higher carrier uptake in hyperplastic or otherwise "activated" sentinel nodes. Potentially, this can be used for targeted loading of the affected and sentinel nodes with high drug doses.

The largest fraction of the carrier collected in lymph nodes is localized in phagocytes. Carrier uptake by lymphatic phagocytes is mediated by multiple interface poly-α-D-glucose chains, while other (internal) carrier components are not essential for the lymphatic uptake. Several prior studies, as well as our own experiments,[7] showed that single dextran B-512 molecules of any size are not effectively recognized by phagocytes or any known lectins, and do not significantly accumulate in lymph nodes. On the contrary, dextran B-512 is considered to be one of the most "biologically inert" polymers.[24] The difference in the interactions of dextran brushes and single dextran molecules with cells appears to be purely quantitative; however, the results of these interactions in vivo are remarkably different. This suggests that at least one strong cooperative effect is present in the phagocyte interactions with multiple poly-α-D-glucose chains. For example, the presence of several chains in the carrier-to-cell contact zone enables summation of binding energy, which must result in an exponential increase in the association constant. Alternatively, cell interaction with a number of molecules is known to trigger endocytosis more efficiently than with a single molecule. Both effects can play a role in nanocarrier accumulation in lymph nodes, which can be mediated by multiple simultaneous low-energy interactions with various surface lectins.

The dose independence and low level of hepatic accumulation suggest that hepatic phagocytes are remarkably inefficient in the recognition and uptake of nanoparticles of this type, as compared to lymphatic phagocytes. Most likely, this is due to significant differences in phagocyte populations residing in these organs, which is to be investigated in future studies of poly-α-D-glucose interaction with lymphatic lectins.

Conclusion

The observed accumulation of poly-α-D-glucose based 10−15 nm nanocarriers in lymphatic phagocytes, in particularly in cells harboring inhaled microparticles and in their near vicinity, presents a significant practical opportunity for infection therapy and prevention. The role of lymph nodes in cancer spread and HIV proliferation provides another strong reason for developing systemic routes for lymph node loading with therapeutic agents.

Nanocarrier feasibility for drug transport to lymphatic phagocytes depends on the availability of carriers with drug-independent or at least nearly independent biokinetics. Such independence can be achieved through drug incorporation into the inner, sterically protected carrier compartment that can be engineered even in a small 10−15 nm particle.

Availability of a suitable drug release mechanism is another requirement directly relevant to the efficacy of an intranodally localized drug. Due to the high lysosomal activity in phagocytes, drug release can possibly rely on hydrolase activity or (in view of the low lysosomal pH) on acid-assisted hydrolysis. The effect of such release systems on the intranodal drug distribution will be evaluated in our ongoing studies.

Depending on the chemical nature of the drug, phagocytes potentially can be used as an intermediate compartment for drug delivery to other intranodal cells. This will depend on the membrane permeability to the intracellularly released drug molecule, and drug ability to diffuse or otherwise translocate through 1−10 cell layers which typically separate intranodal phagocytes from other cells. In oncology, intralymphatic delivery of therapeutic radionuclides with relatively long emitted particle diffusion in tissues, e.g., β and some positron emitters, may be an alternative for radiological postoperative prevention and/or treatment of lymphatic metastases.

Acknowledgment. This research was supported by NIH grants R41 AI052921 and T32 GM07035 and by internal funds of Massachusetts General Hospital. Authors take this opportunity to thank Drs. T. Brady and R. Weissleder for many valuable discussions and Vera Papisov for assistance in editing the manuscript.

MP0499149

---

(23) Yoffey, J.; Courtice, F. *Lymphatics, lymph and the lymphomyeloid complex*; Academic Press: London, 1970.

(24) Larsen, K. Dextran prodrugs—structure and stability in relation to therapeutic activity. *Adv. Drug Delivery Rev.* **1989**, *3*, 103−154.